PHYSICAL REVIEW E **89**, 053106 (2014)

Inhibition of turbulence in inertial-confinement-fusion hot spots by viscous dissipation

C. R. Weber,[*] D. S. Clark, A. W. Cook, L. E. Busby, and H. F. Robey
Lawrence Livermore National Laboratory, Livermore, California 94550, USA
(Received 15 January 2014; published 27 May 2014)

Achieving ignition in inertial confinement fusion (ICF) requires the formation of a high-temperature (>10 keV) central hot spot. Turbulence has been suggested as a mechanism for degrading the hot-spot conditions by altering transport properties, introducing colder, mixed material, or reducing the conversion of radially directed kinetic energy to hot-spot heating. We show, however, that the hot spot is very viscous, and the assumption of turbulent conditions in the hot spot is incorrect. This work presents the first high-resolution, three-dimensional simulations of National Ignition Facility (NIF) implosion experiments using detailed knowledge of implosion dynamics and instability seeds and including an accurate model of physical viscosity. We find that when viscous effects are neglected, the hot spot can exhibit a turbulent kinetic energy cascade. Viscous effects, however, are significant and strongly damp small-scale velocity structures, with a hot-spot Reynolds number in the range of only 10–100.

DOI: 10.1103/PhysRevE.89.053106 PACS number(s): 52.57.−z, 51.20.+d, 52.35.Ra

Experiments at the National Ignition Facility (NIF) [1] seek to compress a capsule (1.11 mm radius), consisting of deuterium-tritium (DT) fuel and an outer plastic (CH) ablator, to sufficient temperatures and densities that a self-sustaining thermonuclear burn is achieved. At the time of ignition, the fuel should be assembled into a low-density (~ 100 g/cm^3), high-temperature (>10 keV) central hot spot surrounded by high-density (~ 1000 g/cm^3) DT fuel. To achieve this goal of inertial confinement fusion (ICF), NIF is using an indirect drive configuration [2], where 192 laser beams irradiate the inner wall of a high-Z hohlraum, surrounding the centrally located capsule with a bath of x-ray radiation at a temperature of up to 300 eV. The outer layers of the capsule ablate and launch a series of shocks inward. Perturbations on capsule surfaces can grow in amplitude and, if sufficiently large, could break up the ablator or mix higher Z material with DT fuel, and thereby cool the central hot spot. Greater-than-expected perturbation growth is one of the possible reasons that NIF experiments have yet to achieve ignition [3,4].

The most comprehensive understanding of a particular experiment comes through detailed postshot modeling [5] using the radiation hydrodynamics code HYDRA [6]. This modeling effort incorporates a wide range of the actual conditions of a particular experiment, including capsule metrology, surface roughness, and radiation drive asymmetry. The strength of the radiation drive is tuned to match the measured shock velocity history [7], the capsule implosion dynamics [8], the bang time (the time of peak neutron production), and the column density (ρR) [9] from several specialized experiments. For some implosions, postshot modeling can produce good agreement with the measured hot-spot size, temperature, and the column density of the fuel, yet the neutron yield is overpredicted by a factor of several ($\sim$2–3×) [5,10]. In some poorly performing experiments, the discrepancy with the simulation is much larger ($>10\times$) and measurements show [3,4] that ablator material is mixing into the hot spot in much greater amounts than the simulations predict.

These discrepancies raise the question of what effects are being left out of the modeling effort. Multiple theories exist to explain these discrepancies. These include a greater influence of low mode asymmetries [11], greater than expected ablation front perturbation growth leading to injected mix [12], and unresolved turbulent behavior in the hot spot that leads to enhanced mix and transport [13,14]. Here we focus on this last theory and show, using the most complete and detailed model of an ICF implosion to date, that turbulent motion cannot be supported in the hot spot and therefore cannot explain the modeling discrepancy.

The theory that turbulence is disrupting the hot spot was recently advanced through simulation by Thomas and Kares [15], which showed that, at very high resolution, turbulence can develop in the interior of a model ICF problem, and they speculated that this could result in ignition failure. Turbulence could cool the hot spot by enhancing mixing and conduction between the hot and cold DT. A turbulent flow field could also contain energy that has not converted into internal energy. Indeed static thermodynamic modeling of NIF implosions suggest that $\sim$3 kJ of energy remains as residual kinetic energy for some experiments [16]. This is larger than simulations predict ($\sim$1 kJ) [5] and larger than bulk velocity measurements can explain [17], thus leaving the possibility of turbulent flows.

With this motivation, this work presents 3D capsule simulations using a different hydrodynamics code, Miranda [18,19], with conditions that adhere as closely as possible to those set forth in the HYDRA postshot modeling effort [5]. The Miranda code was chosen to elucidate the effects of turbulence and mixing, as the code uses 10th-order spatial accuracy with a fixed Eulerian mesh and employs large eddy simulation modeling of subgrid-scale turbulent dissipation. Importantly, Miranda includes models of physical diffusion and viscosity, of which the latter was found crucial in accurately capturing the hot-spot dynamics.

The early stage of the implosion is necessarily simulated using HYDRA, as multigroup radiation diffusion, Lagrangian grid motion, and spherical coordinates are important in resolving the ablation front dynamics. The Miranda cases discussed here, in contrast to HYDRA, did not include radiation transfer

---

[*] weber30@llnl.gov

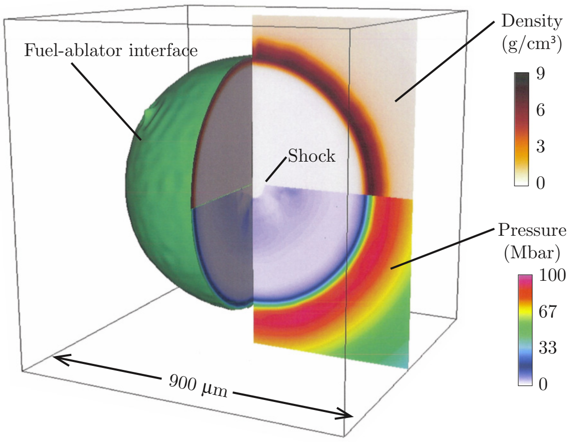

FIG. 1. (Color online) Simulation setup in Miranda showing the 900 μm extent of the domain, the fuel-ablator interface of the capsule, and slices of density and pressure.

or thermonuclear burn. Therefore the Miranda simulation is initialized from the results of the HYDRA simulation once the shocks have broken out of the shell and the perturbations have grown in amplitude but remain linear [20]. At this time the material, density, ion temperature, and velocity data in the central (900 μm)^3 box of the HYDRA simulation are imported into Miranda to start the simulation. As shown in Fig. 1, at this time (21.66 ns) the shell has compressed to 340 μm, the shock has nearly reached the center, and the perturbations are on the order of 1 μm in amplitude. In this example, the HYDRA simulation was modeling NIF shot N120205 and included the measured outer surface perturbations up to mode 50, the observed DT fuel surface defects, and measured broad-mode power spectrum roughness on the fuel and inner ablator surfaces. The 3D x-ray drive asymmetries from a 3D hohlraum simulation were incorporated into the radiation source.

The Miranda simulation is using 512^3 uniformly spaced grid points. To retain resolution of the capsule as it converges, the simulation grid is refined approximately every 50 ps during the course of the simulation. In this process the outer ~6% of the domain is discarded, and the problem is conservatively divided up onto a new 512^3 grid with increased resolution. In this way, the grid spacing starts at 1.75 μm and decreases to 0.5 μm by bang time. A simulation run on a 1024^3 grid without this refinement strategy showed nearly identical final results.

We first show that, without viscosity, both HYDRA and Miranda show a remarkably high level of agreement. This is notable given the complexity of the flow and the significantly different numerics of each code. By bang time (22.7 ns) the fuel-ablator interface has converged from a radius of 340 μm to 54 μm. Figure 2 shows density and velocity fields from a plane slicing through the capsule center. The Miranda simulation consists of approximately 256 grid cells across the width of the image, which is sufficient to resolve all preimposed perturbations. The HYDRA simulation's nonuniform mesh has approximately twice the resolution in the interior of the capsule compared to the Miranda simulation. The density field from the Miranda and HYDRA simulations show a very similar shape, with 10 individual high-density spikes penetrating towards the center of the capsule. The interface between DT and ablator material is displayed as a white dashed line, showing that perturbations on this interface do not inject ablator material into the hot spot. The hot spot, identified here as the 1 keV boundary and shown in Fig. 2 as a black dashed line, takes the shape of the inner surface of the DT fuel.

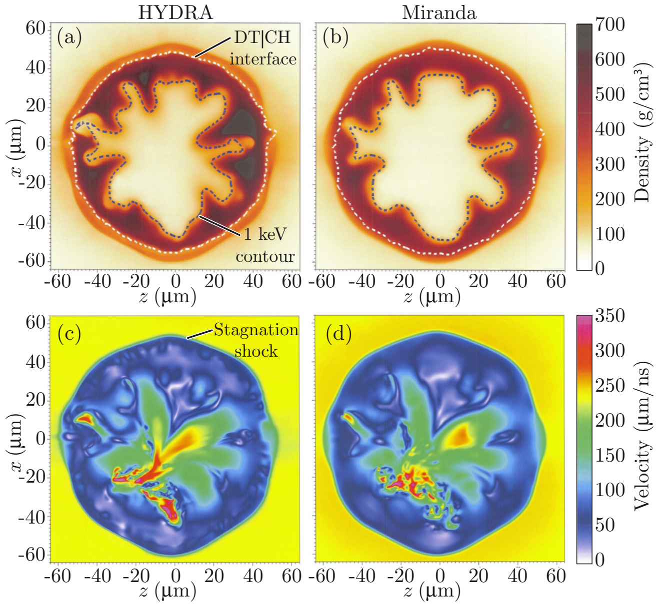

FIG. 2. (Color online) Density (top) and velocity (bottom) slice from HYDRA (left) and Miranda (right) at bang time. The white contour on the density images shows the location of the fuel-ablator interface, and the black contour shows the 1 keV boundary.

The lower half of Fig. 2 shows the velocity magnitude at bang time. Both HYDRA and Miranda show high-velocity features present in the hot spot. At upwards of 350 μm/ns, these low-density jets are comparable to the peak implosion velocity of the fuel. At this time, HYDRA and Miranda compute 0.71 and 0.69 kJ of kinetic energy remains in the DT, respectively. These similarities lend confidence to the reliability of each model. The question of whether higher resolution would produce increased hot-spot turbulence, however, remains open. To this point, we next show that these simulations are effectively overresolved due to the absence of physical viscosity modeling.

With the high temperatures in the hot spot, viscous effects become important at these small scales. To demonstrate this, an additional Miranda simulation is presented, identical to the previous case, except including a physical viscosity model. Figure 3 shows the 4π-averaged profiles of several parameters at the time of peak fuel kinetic energy (22.41 ns). Notice that at this time the stagnation shock is entering the high-density fuel. Temperatures in the hot spot reach 2.3 keV. The thermodynamic regime of the plasma is governed by the plasma coupling parameter, $\Gamma = (Z_i e)^2/a k_B T$, where $Z_i e$ is the ionic charge, a is the ionic sphere radius, and $k_B T$ is the ionic temperature. This parameter represents the ratio of potential energy from Coulombic interactions to the thermal energy. When this value is very small, the viscosity can be described by kinetic theory [21]. Above the weakly coupled regime ($\Gamma > 0.5$), molecular dynamics (MD) simulations are

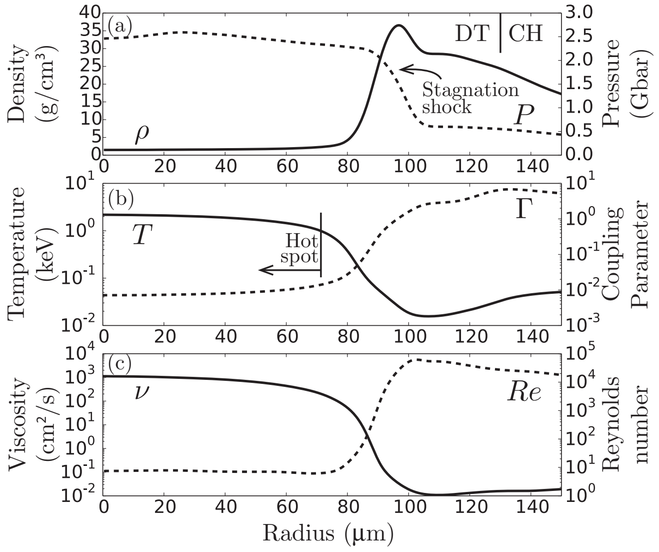

FIG. 3. Radial profiles, averaged over 4π, at the time of peak fuel kinetic energy. (a) Density and pressure, (b) temperature and plasma coupling parameter, and (c) kinematic viscosity and Reynolds number. Solid curves correspond to the left axis, dashed curves correspond to the right axis.

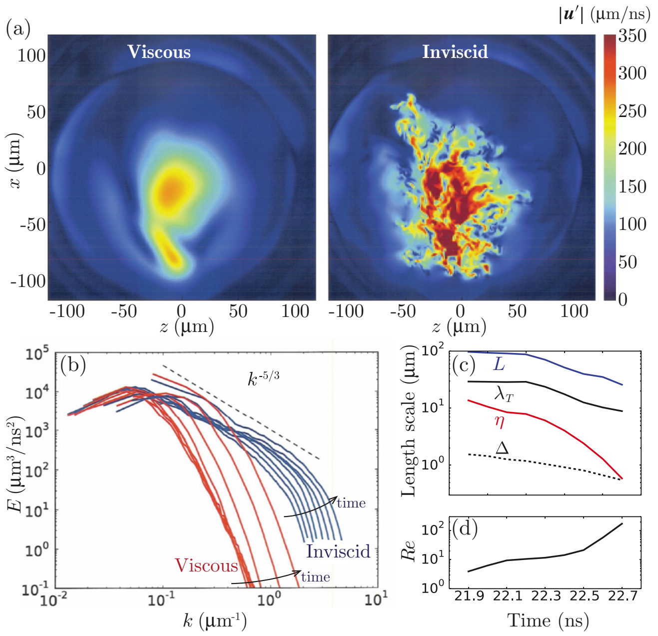

FIG. 4. (Color online) Viscous effects on the fluctuating velocity. (a) Fluctuating velocity magnitude at 22.21 ns with (left) and without (right) viscosity. (b) Kinetic energy spectra in the hot spot from the viscous and inviscid simulations from 21.9 to 22.6 ns. (c) Turbulent length scales and (d) Reynolds number from the hot spot.

often relied upon to model the viscosity. Figure 3(b) shows that Γ is approximately 0.01 in the low-density hot spot and 1–10 in the higher-density DT fuel and CH ablator. The viscosity model implemented in Miranda for the current simulations uses the results of MD simulations of a Yukawa system [22] and corrected to asymptote to the kinetic regime at low Γ [21]. The kinematic viscosity, shown in Fig. 3(c), varies by five orders of magnitude from the hot spot to the ablation front.

The Reynolds number of the hot spot is given by $\mathrm{Re} = |\boldsymbol{u}'|L/\nu$, where the fluctuating velocity is taken as the nonradial velocity, $\boldsymbol{u}' = \boldsymbol{u} - U(r)$, and $U(r)$ is the 4π-averaged radial velocity profile. For a length scale, the wavelength of mode 10 is used, $L = 2\pi r/10$, as it is the dominant perturbation of the inner fuel surface at late times. The Reynolds number, shown in Fig. 3(c), ranges from 8 in the hot spot to 2×10^4 near the fuel-ablator interface. This low Reynolds number implies that, even if these estimates of viscosity or length scale are in error by an order of magnitude, the viscous effects in the hot spot will still be considerable.

When viscous effects are included in the simulation, they act to dissipate small-scale velocity structures that are present in the hot spot. Figure 4(a) shows the nonradial velocity magnitude at 22.21 ns (0.2 ns before peak fuel kinetic energy) from the Miranda simulations with and without viscous effects. The dramatic smoothing of the velocity field in the presence of viscosity is evident. Others have noted the influence of viscosity in suppressing Rayleigh-Taylor growth and smoothing the shock front in the low-density interior of the capsule [23–26], but this is the first recognition of its role in limiting small-scale motion in the hot spot.

The 3D turbulent kinetic energy spectra are shown in Fig. 4(b). These spectra use the fluctuating velocity fields and are computed within a box centered on the hot spot with sides that extend to the high-density fuel. The spectra are computed from both the viscous and inviscid cases and at several times from 21.9 to 22.6 ns. The spectra show a much wider range of scales in the inviscid case, with the possible emergence of a turbulent $k^{-5/3}$ inertial range [27] at the latest time. The high wave-number region in the inviscid case shows the effects of artificial viscosity, which removes kinetic energy near the grid scale [18]. Physical viscosity, however, removes energy at much larger scales, as seen by the steeper dropoff in the viscous kinetic energy spectra.

Several characteristic length scales are extracted from the viscous simulation and are shown in Fig. 4(c). The largest is the integral length scale, $L = \frac{3\pi}{2}\int k^{-1}E\,dk/\int E\,dk$, where $|\boldsymbol{u}'|^2 = \frac{3}{2}\int E\,dk$, followed by the Taylor microscale, $\lambda_T = (15\nu|\boldsymbol{u}'|^2/\varepsilon)^{1/2}$, where the dissipation is $\varepsilon = \int 2\nu k^2 E\,dk$, and finally the Kolmogorov scale, $\eta = (\nu|\boldsymbol{u}'|^3/\varepsilon)^{1/4}$ [27]. All length scales decrease in time due to the compression of the capsule. The Kolmogorov length scale, which is effectively the smallest scale of the flow, ranges from 10 μm in the beginning of the simulation to 0.6 μm by bang time. The grid spacing of the simulation, Δ, is also shown in Fig. 4(c) and is much smaller than the Kolmogorov scale for most of the simulation. A resolution of $\Delta \lesssim 2.1\eta$ is necessary to capture nearly all of the energy of the flow [27]; therefore even at bang time, when the Kolmogorov and grid scales are approximately equivalent, all of the length scales in the hot spot are well resolved. The Reynolds number of the hot spot, computed here using the integral length scale and the rms velocity, $|\boldsymbol{u}'|$, is shown in Fig. 4(d). For much of the duration of the simulation it is on the order of Re $\sim$10. The increase in Re near the end of the simulation (Re $\approx$ 170 at bang time) is due to the increase in the density of the hot spot, which reduces the kinematic viscosity,

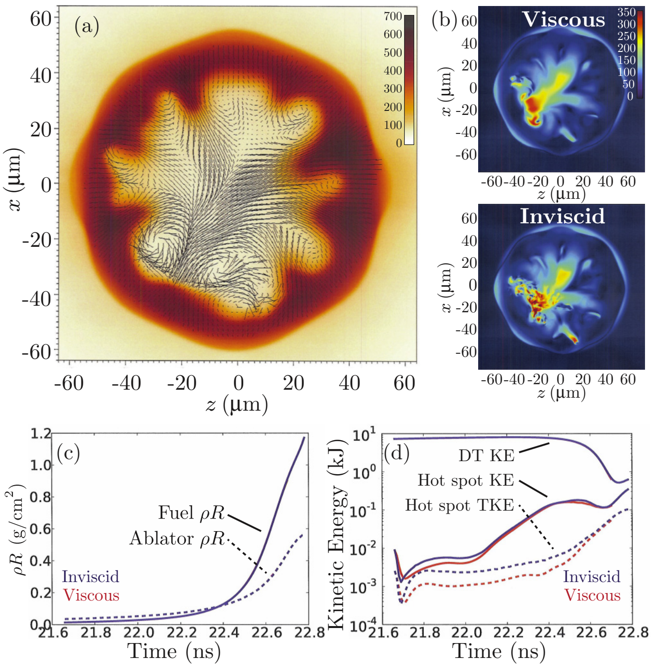

FIG. 5. (Color online) Viscous effects at bang time on density, velocity, and integrated quantities. (a) Density and velocity vectors from the viscous simulation (vectors are only shown in the DT material for clarity). (b) Fluctuating velocity from the viscous (top) and inviscid (bottom) simulations. (c) Fuel and ablator ρR. (d) Kinetic energy from all of the DT, from the hot spot, and turbulent (nonradial) kinetic energy in the hot spot. Each quantity in (c) and (d) has a viscous (red) and inviscid (blue) curve, but some viscous curves are hidden by the inviscid curves.

and the increase of nonradial kinetic energy in the hot spot during stagnation.

While viscosity has a significant effect on velocity fluctuations during the formation of the hot spot, the overall picture of the flow field at bang time is not changed significantly. Figure 5(a) shows the density field from the viscous simulation with superposed velocity vectors. Compared with the inviscid simulation [Fig. 2(b)], viscosity slightly reduces the penetration of the fuel spikes into the hot spot, with some spikes reduced by ∼5 μm. The overall concentration of mass, shown in Fig. 5(c) as fuel ρR and ablator ρR, is nearly identical for the inviscid and viscous case, as the two curves lie on top of each other. The fluctuating velocity fields, shown in Fig. 5(b), are also similar at bang time. The inviscid case shows smaller-scale structures near the peak-velocity region, but outside this location the flow fields are nearly the same. Figure 5(d) shows the kinetic energy versus time, divided up into the kinetic energy of all of the DT (top curve), the kinetic energy of the hot spot ($T < 1$ keV, middle curve), and the turbulent (nonradial) kinetic energy (TKE) in the hot spot (bottom dashed curve). Between the start of the simulation and the time of peak fuel kinetic energy (22.41 ns), the viscous case has ∼2× less TKE as the inviscid case. After this period, both the inviscid and viscous cases experience a rapid increase in hot-spot TKE, eventually reaching similar values at bang time.

The vector field in Fig. 5(a) demonstrates why both cases experience a similar increase in TKE near the end of the implosion. As the high-density fuel stagnates and becomes Rayleigh-Taylor unstable, spikes fall into the hot spot and push jets of material through the interior. Figure 5(a) shows that the direction of these jets are well correlated with the fuel spikes entering the hot spot. Thus there exists two sources of hot-spot TKE. The first is the initial shock waves, whose distortions lead to small-scale vorticity deposition. Viscous dissipation removes much of this kinetic energy. The second source of hot-spot TKE is the inner surface of the high-density fuel, which pushes material in front of it during stagnation. Having a low-mode shape, this inner surface produces low-mode kinetic energy, which is not as affected by viscous dissipation.

In summary, using the most complete and detailed model of an ICF capsule implosion currently available, this work shows that viscous dissipation prevents the formation of turbulence in the hot spot during ICF implosions. This rules out hot-spot turbulence as a possible source for failed performance. Viscosity strongly damps the small-scale velocity structure that is deposited by shocks reverberating in the interior of the capsule. Prior to fuel stagnation, the hot spot has a Reynolds number near 10. The additional energy and increase in density during stagnation raises the Reynolds number to near ∼100, which is in contrast to the turbulent energy cascade seen in the inviscid simulation. The Kolmogorov length scale of 1–10 μm indicates that ICF simulations with greater resolution than this will have an inaccurate picture of the flow if viscous effects are neglected. While the inclusion of viscous effects does not alter the averaged properties of the hot spot, the fine-scale, detailed structure of the flow is significantly smoothed by the inclusion of physical viscosity.

We wish to thank Dr. W. H. Cabot for his work on modeling plasma properties in the Miranda code. This work was performed under the auspices of the U.S. Department of Energy by Lawrence Livermore National Laboratory under Contract No. DE-AC52-07NA27344.

---

[1] M. J. Edwards *et al.*, Phys. Plasmas **20**, 070501 (2013).

[2] J. D. Lindl, P. Amendt, R. L. Berger, S. G. Glendinning, S. H. Glenzer, S. W. Haan, R. L. Kauffman, O. L. Landen, and L. J. Suter, Phys. Plasmas **11**, 339 (2004).

[3] S. P. Regan *et al.*, Phys. Plasmas **19**, 056307 (2012).

[4] T. Ma, P. K. Patel, N. Izumi, P. T. Springer, M. H. Key, L. J. Atherton, L. R. Benedetti, D. K. Bradley, D. A. Callahan, and P. M. Celliers, Phys. Rev. Lett. **111**, 085004 (2013).

[5] D. S. Clark *et al.*, Phys. Plasmas **20**, 056318 (2013).

[6] M. M. Marinak, G. D. Kerbel, N. A. Gentile, O. Jones, D. Munro, S. Pollaine, T. R. Dittrich, and S. W. Haan, Phys. Plasmas **8**, 2275 (2001).

[7] H. F. Robey *et al.*, Phys. Plasmas **19**, 042706 (2012).

[8] D. G. Hicks, N. B. Meezan, E. L. Dewald, A. J. Mackinnon, R. E. Olson, D. A. Callahan, T. Döppner, L. R. Benedetti, D. K. Bradley, and P. M. Celliers, Phys. Plasmas **19**, 122702 (2012).

[9] S. H. Glenzer *et al.*, Phys. Plasmas **19**, 056318 (2012).

[10] D. S. Clark *et al.*, Bull. Am. Phys. Soc. **58**, 362 (2013).

[11] R. H. H. Scott *et al.*, Phys. Rev. Lett. **110**, 075001 (2013).

[12] S. P. Regan, R. Epstein, B. A. Hammel, L. J. Suter, H. A. Scott, M. A. Barrios, D. K. Bradley, D. A. Callahan, C. Cerjan, and G. W. Collins, Phys. Rev. Lett. **111**, 045001 (2013).

[13] D. C. Wilson, A. J. Scannapieco, C. W. Cranfill, M. R. Clover, N. M. Hoffman, and J. Collins, Phys. Plasmas **10**, 4427 (2003).

[14] Technical Report LLNL-TR-570412, Lawrence Livermore National Laboratory, 2012.

[15] V. A. Thomas and R. J. Kares, Phys. Rev. Lett. **109**, 075004 (2012).

[16] C. Cerjan, P. T. Springer, and S. M. Sepke, Phys. Plasmas **20**, 056319 (2013).

[17] M. Gatu Johnson *et al.*, Phys. Plasmas **20**, 042707 (2013).

[18] A. W. Cook, Phys. Fluids **19**, 055103 (2007).

[19] A. W. Cook, Phys. Fluids **21**, 055109 (2009).

[20] D. S. Clark, S. W. Haan, A. W. Cook, M. J. Edwards, B. A. Hammel, J. M. Koning, and M. M. Marinak, Phys. Plasmas **18**, 082701 (2011).

[21] S. I. Braginskii, Rev. Plasma Phys. **1**, 205 (1965).

[22] M. S. Murillo, High Energy Density Phys. **4**, 49 (2008).

[23] K. O. Mikaelian, Phys. Rev. E **47**, 375 (1993).

[24] H. F. Robey, Phys. Plasmas **11**, 4123 (2004).

[25] D. Li, I. Igumenshchev, and V. Goncharov, Bull. Am. Phys. Soc. **51**, 342 (2006).

[26] W. Manheimer and D. Colombant, Laser Particle Beams **25**, 541 (2007).

[27] S. Pope, *Turbulent Flows* (Cambridge University Press, Cambridge, 2000).